The Detection of Wind-Turbine Noise in Seismic Records

Article *in* Seismological Research Letters · September 2018

DOI: 10.1785/0220170271

CITATIONS
24

READS
331

2 authors, including:

Joshua Carmichael
Los Alamos National Laboratory
41 PUBLICATIONS **235** CITATIONS

SEE PROFILE

LA-UR-17-30303
Approved for public release; distribution is unlimited.

Title: The detection of wind-turbine noise in seismic records

Author(s): Marcillo, Omar Eduardo
Carmichael, Joshua Daniel

Intended for: Bulletin of the Seismological Society of America

Issued: 2017-11-09 (Draft)

The detection of wind-turbine noise in seismic records.

Omar E. Marcillo and Joshua Carmichael

Los Alamos National Laboratory

Corresponding author:

Omar E. Marcillo

Los Alamos National Laboratory

Mailing address:

P.O. Box 1663

MS D446

Los Alamos, NM 87545

omarcillo@lanl.gov

Abstract

Large wind turbines (WTs) can produce noise observable from the ground or atmosphere up to10s of km from the source. Like other machinery with rotating blades (e.g., helicopters and large fans), WTs can generate noise characterized by sharp spectral peaks centered at the blade-passing frequency and its integer harmonics (F&H noise). We quantify a methodology to detect F&H noise in seismic records by estimating fundamental frequencies and its harmonic sequences. We test the performance of this algorithm by analyzing several years of seismic data recorded on two stations of the US Seismic Network in Texas (US). The blade passing frequency for most modern WTs (> 1MW) is around 1Hz as new turbine development favors increasing blade size and decreasing rotational frequency. Such WT noise is distinct from typical background noise as it is easily masked in seismic noise studies after traditional smoothing algorithms. As wind turbine proliferation spreads globally, such signatures will become increasingly present in seismic records and their monitoring may help quantify seismic station performance and site characterization.

1. Introduction

Wind continues to present one of the fastest growing renewable energy sources in the United States (US) since the year 2000. In particular, the US produced about 25 GWh (Wh denotes Watt-hour) of power in March 2017 relative to 0.5 GWh in March 2001 (U. S. Energy Information Agency, EIA). Wind energy capacity in the US is unevenly distributed, with production largely concentrated in Texas, Iowa, Oklahoma, California, and Kansas, which accounts for >50% of US wind capacity. Among these states, Texas has the peak energy potential at ~17% of the total potential of onshore capability (Lopez, Roberts et al. 2012). Specifically, Texas hosts 129 wind projects comprised of nearly 12,000 operational wind turbines (WTs) as of December 2016 (American Wind Energy Association AWEA) . These turbines are a known source of both acoustic and seismic energy, but how the operation of these WTs drives seismic background noise as well as whether WTs produce a quantifiable signature that dominates their region of proliferation remains unclear. The increasing distribution of WTs thereby presents a topical research challenge for quantifying the growth and spatial distribution of anthropogenic background noise. Furthermore, such noise may serve as an imaging tool for passive seismic studies. To address this challenge, we use high fidelity seismic stations that record the ground motion signatures of these WTs. We use this data to describe a methodology to detect and characterize their seismic signature, and demonstrate its utility using two seismic stations that have operated in TX since 2004. Our method thereby gives a quantitatively defensible procedure to monitor WT operation.

1.1. Seismic Signatures of Wind Turbines.

WTs convert kinetic energy from atmospheric wind into electric energy by driving rotating blades around a rotor. WTs are commonly deployed together in groups known as wind farms (WFs). WTs operate under different configurations (Arturo Soriano, Yu et al. 2013, Hau and Von Renouard 2013) with modern WTs composed of three blades and a horizontal axis. The rotation speed of a particular WT can be fixed or variable. Seismic and acoustic signatures of WTs that operate at a fixed frequency of rotation display a very distinct spectrum characterized by peaks centered at a fundamental frequency and its integer harmonics. This signature is observable from several 10s of kilometers in seismic (Stammler and Ceranna 2016) and acoustic records (Marcillo, Arrowsmith et al. 2015). Stammler and Ceranna (2016) studied this signature to determine its influence on the performance of a seismic array located in Germany and operated by the Comprehensive Test Treaty Organization International Monitoring System (CTBT-IMS). Others (Saccorotti, Piccinini et al. 2011, Gortsas, Triantafyllidis et al. 2017) have conducted similar studies near a gravitational wave observatory to identify any effect WTs noise had upon their measurements. None of these studies focused on a detection methodology to characterize the WTs signatures.

2. Data and methods

We analyzed seismic data from the vertical component of two, three-component broad-band stations, AMTX (Amarillo, Texas, US) and NATX (Nacogdoches, Texas, US), included within the US Seismic Network. Both stations continuously record ground motion data at 40 samples per second which is then archived at the IRIS Data

Management Center (IRIS-DMC) repository. AMTX and NATX have recorded continuously since 2004 with brief punctuations in uptime. Station AMTX is installed at the highest wind energy potential location in the state, while NATX is installed at the lowest wind energy potential location. These locations thereby provide ostensible upper and lower bounds in expected WTs noise generation (Figure 1).

2.1. A detector for energy peaks with harmonics.

We previously applied a peak energy detector (Marcillo, Arrowsmith et al. 2015) to identify the signature of a WF in central New Mexico with 60 WT using acoustic measurements at distances in the 10s of km. We now generalize the same detector to identify multiple unknown peaks. Conceptually, this detector operates in three stages by (1) normalizing the signal to prevent the interference of transients, (2) estimating the power spectral density (PSD) of the signals and identifying peaks in their spectrum, and (3) categorizing peaks within a sequence that includes a fundamental and multiple corresponding integer harmonics

(1) **Waveform temporal normalization.** To reduce the influence of earthquakes and other transient signals (of short duration) that can distort PSD estimations, we apply a waveform temporal normalization following the method of Bensen, Ritzwoller et al. (2007). We perform this normalization at each sample (d_i) using an rms normalization: $\widetilde{d_i} = d_i/\omega_i$ (Bensen, Ritzwoller et al. 2007), with:

$$\omega_i = \frac{1}{2N+1}\sqrt{\sum_{j=i-N}^{i+N} {d_j}^2} \qquad \text{Equation 1}$$

where N is the number of samples before and after each point. Section A.1 of the supplementary material demonstrates that for large N, assuming that d_i is normally distributed, $\widetilde{d}_i$ is also normally distributed. Figure 2 shows the effect of normalization in in the estimation of PSDs (panels b and d) for a record contaminated with a large transient event (around 8:30). Panel b shows both PSDs before (black) and after (blue) normalization.

(2) **Energy-peak identification.** The second stage of the algorithm identifies energy peaks in the PSD of the normalized time series. We use the Welch (1967) method to estimate the PSD on waveform segments of length W using W/L sub-windows of length L. Next, we compute rolling statistics, i.e., mean and standard deviation, using rolling windows of length F for all elements of the PSD so each frequency point has a PSD value (v_i), mean (m_i), and standard deviation (σ_i). The algorithm identifies frequencies peaks by comparing the values v_i to a threshold $h_i = m_i + n \cdot \sigma_i$ using $v_i > h_i$, where n is an integer. For frequencies components above the threshold, the value v_i is replaced by m_i, and new rolling statistics are computed. A new set of peaks is found using a new threshold built with the updated rolling statistics. The replacement-update-peak identification sequence is intended to reduce the influence of adjacent large frequency peaks that can bias the rolling statistics and lower the sensitivity of the algorithm. This sequence can be repeated multiple times. Figure 2 panels b and d show examples of this stage with identified peaks (magenta dots) superimposed on the PSD estimations. Appendix A.2 assesses the statistical performance of this stage of the algorithm by estimating the probability of detection of a pure sinusoid with limited lifespan.

(3) **Fundamental and harmonics (F&H) sequence identification.** The third stage of the algorithm categorizes the peaks and builds F&H sequences. The algorithm starts by sorting the peaks in ascending order of frequency. Assuming the peak with lowest frequency (ξ) is a fundamental, the algorithm looks for other peaks in the list that follow the sequence: $2 \cdot \xi, 3 \cdot \xi, \ldots, \mathrm{H} \cdot \xi$, where H is an integer. If a sequence with at least η consecutive peaks (including the fundamental) are found, the algorithm declares the detection of a F&H sequence. If a F&H sequence is detected, the peaks of the sequence are removed from the list and the algorithm starts again with the new lowest peak. The probability of the detection of a F&H sequence is estimated as the product of the probability of the detection of individual energy peaks (see Appendix A.3) .

Figure 3 shows the results of the algorithm with different configurations for n applied to a 6-hour record for station AMTX. Our algorithm first normalized the illustrated waveform using N =120 (for stage 1) which corresponds to a 3-second normalization window before and after each point of the waveform. The algorithm then estimates the PSD with W = 6 h with sub-windows with L=0.5 h and 75% overlap. The estimated PSD for this waveform shows three clear peaks between 0.5 and 0.9 Hz. The algorithm is configured with $n = 3$ and $\eta = 2$ detects four fundamental peaks in the 0.5-0.9 Hz band within F&H sequences. With $n = 2$ and $\eta = 2$ the algorithms detects more than 10 F&H

149 sequences. This particular configuration detects sequences that are less visible as F&H
150 sequences.
151
152 **3. RESULTS**
153 We applied our detector to all IRIS DMC data available from 2004 to 2017 at stations
154 AMTX and NATX. We use W = 6 h and a step of 3 h, $L = 0.5$ h and 75% overlap. We
155 restricted peak detections to sequences with a fundamental frequency and at least two
156 harmonics. By restricting the detection to two harmonics, we observed a significant
157 decrease in the number of false detections. Figure 4 shows our results from 12 years of
158 data collected at both stations. Time periods following 2007 at AMTX show a clear
159 pattern of fundamental frequency detection near 0.8 Hz up to a third harmonic is visible
160 following the 0.8 Hz peak. A second frequency peak slightly above 0.9 Hz then appears
161 during early 2009. A third peak appears in mid 2012 slightly below 0.9 Hz. Three more
162 peaks are detected in late 2014, mid 2015 and late 2016 at around 0.85, 0.75, and 0.7 Hz
163 (respectively). Note that these five fundamental peaks are the same showed in Figure 3.
164 Station NATX does not show any particular pattern in the detection of frequencies.
165
166 Figure 5 shows histograms of the detections for both stations as a function of the time of
167 day. The histogram for AMTX shows a significant increase in the detection of F&H-
168 noise between 0 and 12 hours, which corresponds to local hours 6pm to 6am. This
169 enhanced detectability at night hours either relates to lower local site noise or increased
170 wind farm activity during the night.
171

4. DISCUSSION

The window length (W) and sub-window length (L) used in the construction of the PSDs at stage 2 of our detector have a significant effect on the performance of the detector. Large W allows for higher frequency resolution and a proportionally large number of sub-windows. A high number of sub-windows would attenuate the random noise by incorporating more sub-windows to be averaged, but may also include periods without F&H noise. As the PSD averages these mixed periods, the amplitude of F&H noise (if present) becomes diminished. Large earthquakes and other energetic transient events (e.g.: lightning), when present, can modify the PSD estimations and mask the F&H signals (Figure 2). We selected W=6 h and a step of 3 h between PSDs to ensure at least one estimation samples sections of the day (mostly at night) with low anthropogenic noise (Figure 5).

Most seismic noise studies to date assume that background noise is composed of continuous broadband signals. The noise we describe, triggered by the operation of some types of WTs, is also broadband, because the harmonics can cover a significant portion of the spectrum but does not have a not continuous spectrum. Frequency smoothing, which is commonly used for background noise studies (McNamara and Buland 2004), can significantly distort this specific signature. As WF deployment increases worldwide, WT noise will ostensibly grow increasingly prevalent in seismic records. Therefore, the necessity of seismic monitoring operations to characterize such signals as part of the seismic background noise will increase as will the need to assess their potential impact in the detection and location capabilities of seismic (Stammler and Ceranna 2016) and other

scientific instrumentation (Daw, Giaime et al. 2004, Matichard, Lantz et al. 2015). Figure 6 illustrates WT plant proliferation over 10 prior years (2005 -2015) (ref) along with a concurrent increase in seismic station coverage within the US network. Note that in west and mid-west states the number of wind plants may affect some of the high sensitivity seismic sensors. This characterization is particularly important as new turbines are expected to increase in size and have larger blades with lower rotational speed. These turbine features are exemplified by the General Electric's new Haliade 150-6MW WT, which has operational rotational speeds between 4 and 11.5 rpm.

5. CONCLUSIONS AND FINAL REMARKS

As previously stated, seismic and acoustic signatures of some industrial processes and rotating blade machinery display a very distinct spectrum characterized by peaks centered at a fundamental frequency and its harmonics (F&H noise). Signals with F&H characteristics have been used for the detection and identification of large ground vehicles (Altmann, Linev et al. 2002, Altmann 2004) and helicopters (Damarla and Ufford 2008, Damarla 2010). Signals with these spectral characteristics are also generated in volcanic environments (Dziak and Fox 2002).

The signature of the operation of WTs is observable as seismic waves up to 10s of kilometers from the source. Here, we have developed a methodology specifically designed to detect this harmonic signature and applied it to two seismic stations located in Texas (US) to demonstrate the performance of our detector and compare a station with high concentration of station proximal WTs (within 100 km) to a station with no

proximal WTs. This detector can improve the characterization of site seismic noise which is especially important for highly sensitive instruments, such as LIGO and high fidelity seismic stations, as strategies to mitigate their influence in measurements are directly related to the characteristics of noise. In future work, we will explore the application of our algorithm to monitor small changes in the spectral characteristics of F&H sequences and relate these changes to characteristics of the source, and any changes in structure of the propagation medium.

Data and resources

The seismic data for stations AMTX and NATX and metadata for US seismic stations were retrieved from the IRIS Data Management Center: http://ds.iris.edu/ds/nodes/dmc/. The information from Net Power was retrieved from the U.S. Energy Information Administration website (https://www.eia.gov/)

Acknowledgments

This manuscript has been authored by Los Alamos National Security under Contract Number DE-AC52-06NA25396 with the U.S. Department of Energy. The United States Government retains and the publisher, by accepting the article for publication, acknowledges that the United States Government retains a non-exclusive, paid-up, irrevocable, world-wide license to publish or reproduce the published form of this manuscript, or allow others to do so, for United States Government purposes.

6. References

Altmann, J. (2004). "Acoustic and seismic signals of heavy military vehicles for co-operative verification." Journal of Sound and Vibration **273**(4-5): 713-740.

Altmann, J., S. Linev and A. Weiss (2002). "Acoustic-seismic detection and classification of military vehicles - developing tools for disarmament and peace-keeping." Applied Acoustics **63**(10): 1085-1107.

American Wind Energy Association. "U.S. Wind Energy State Facts." Retrieved June, 2017, 2017, from https://www.awea.org/resources/statefactsheets.aspx.

Arturo Soriano, L., W. Yu and J. d. J. Rubio (2013). "Modeling and control of wind turbine." Mathematical Problems in Engineering **2013**.

Bensen, G. D., M. H. Ritzwoller, M. P. Barmin, A. L. Levshin, F. Lin, M. P. Moschetti, N. M. Shapiro and Y. Yang (2007). "Processing seismic ambient noise data to obtain reliable broad-band surface wave dispersion measurements." Geophysical Journal International **169**(3): 1239-1260.

Damarla, T. (2010). Azimuth & elevation estimation using acoustic array. 2010 13th International Conference on Information Fusion.

261 Damarla, T. R. and D. Ufford (2008). Helicopter detection using harmonics and
262 seismic-acoustic coupling. Proc. of SPIE Vol.

263 Daw, E. J., J. A. Giaime, D. Lormand, M. Lubinski and J. Zweizig (2004). "Long-term
264 study of the seismic environment at LIGO." Classical and Quantum Gravity **21**(9):
265 2255-2273.

266 Diffendorfer, J. E., R. Compton, L. Kramer, Z. Ancona and D. Norton (2017). Onshore
267 industrial wind turbine locations for the United States (ver. 1.2, January 2017): U.S.
268 Geological Survey Data Series 817, USGS.

269 Dziak, R. P. and C. G. Fox (2002). "Evidence of harmonic tremor from a submarine
270 volcano detected across the Pacific Ocean basin." Journal of Geophysical Research:
271 Solid Earth **107**(B5): ESE 1-1-ESE 1-11.

272 Geary, R. C. (1930). "The frequency distribution of the quotient of two normal
273 variates." Journal of the Royal Statistical Society **93**: 442-446.

274 Gortsas, T. V., T. Triantafyllidis, S. Chrisopoulos and D. Polyzos (2017). "Numerical
275 modelling of micro-seismic and infrasound noise radiated by a wind turbine." Soil
276 Dynamics and Earthquake Engineering **99**: 108-123.

277 Hau, E. and H. Von Renouard (2013). Wind turbines: fundamentals, technologies,
278 application, economics, Springer Science & Business Media.

279 Hinkley, D. V. (1969). "On the Ratio of Two Correlated Normal Random Variables."
280 Biometrika **56**(3): 635-639.

281 Kay, S. M. (2013). Fundamentals of statistical signal processing: Practical algorithm
282 development, Pearson Education.

283 Lopez, A., B. Roberts, D. Heimiller, N. Blair and G. Porro (2012). US renewable energy
284 technical potentials: a GIS-based analysis, NREL.

285 Marcillo, O., S. Arrowsmith, P. Blom and K. Jones (2015). "On infrasound generated
286 by wind farms and its propagation in low-altitude tropospheric waveguides."
287 Journal of Geophysical Research: Atmospheres **120**(19): 9855-9868.

288 Matichard, F., B. Lantz, R. Mittleman, K. Mason, J. Kissel, B. Abbott, S. Biscans, J.
289 McIver, R. Abbott, S. Abbott, E. Allwine, S. Barnum, J. Birch, C. Celerier, D. Clark, D.
290 Coyne, D. Debra, R. DeRosa, M. Evans, S. Foley, P. Fritschel, J. A. Giaime, C. Gray, G.
291 Grabeel, J. Hanson, C. Hardham, M. Hillard, W. Hua, C. Kucharczyk, M. Landry, A. Le
292 Roux, V. Lhuillier, D. Macleod, M. Macinnis, R. Mitchell, B. O'Reilly, D. Ottaway, H.
293 Paris, A. Pele, M. Puma, H. Radkins, C. Ramet, M. Robinson, L. Ruet, P. Sarin, D.
294 Shoemaker, A. Stein, J. Thomas, M. Vargas, K. Venkateswara, J. Warner and S. Wen
295 (2015). "Seismic isolation of Advanced LIGO: Review of strategy, instrumentation
296 and performance." Classical and Quantum Gravity **32**(18).

McNamara, D. E. and R. P. Buland (2004). "Ambient noise levels in the continental United States." Bulletin of the Seismological Society of America **94**(4): 1517-1527.

Saccorotti, G., D. Piccinini, L. Cauchie and I. Fiori (2011). "Seismic Noise by Wind Farms: A Case Study from the Virgo Gravitational Wave Observatory, Italy." Bulletin of the Seismological Society of America **101**(2): 568-578.

Stammler, K. and L. Ceranna (2016). "Influence of Wind Turbines on Seismic Records of the Grafenberg Array." Seismological Research Letters **87**(5): 1075-1081.

Welch, P. D. (1967). "The use of fast Fourier transform for the estimation of power spectra: A method based on time averaging over short, modified periodograms." Audio and Electroacoustics, IEEE Transactions on **15**(2): 70-73.

Mailing Addresses

Omar E. Marcillo

Mailing address:

P.O. Box 1663

MS D446

Los Alamos, NM 87545

Joshua Carmichael

Mailing address:

P.O. Box 1663

MS D446

Los Alamos, NM 87545

LIST OF FIGURE CAPTIONS

Figure 1: a) Wind capacity map for the state of Texas (US), location of wind turbines (Diffendorfer, Compton et al. 2017), and location of the two seismic stations used for testing the detection algorithm. b) Region around AMTX with WTs color-coded with the year on starting operations.

Figure 2: Temporal waveform normalization. The PSDs (panels b and d) were both estimated using W=6 h and L=0.5 h, and 75% overlap between sub-windows. The magenta dots show the location of peaks (stage 2) found using rolling statistics (mean and standard deviation) with 120 points, one peak-replacement loop, and n=3.

Figure 3: The influence of the number of standard deviations (s) in energy-peak identification stage of the algorithm. The dots mark the location of the identified fundamental frequency while the plus-symbols mark their harmonics. Fundamentals and corresponding harmonics are linked by color. The colored vertical lines mark the theoretical locations of harmonics at estimated fundamental frequencies.

Figure 4: Detection of F&H noise for stations: AMTX and NATX since year 2005. The Figure shows the number of detection in a 30-day period.

Figure 5: Distribution of peak detections by time of day.

352

353 Figure 6: Distribution of energy plants (WTs with wind power capacity > 1 MW are
354 marked blue) and US Seismic Network stations (magenta dots) for years 2015 (a) and
355 2005 (b). The size of the blue circles is related to the relative amount of energy generated
356 by each power plant.

357

FIGURES

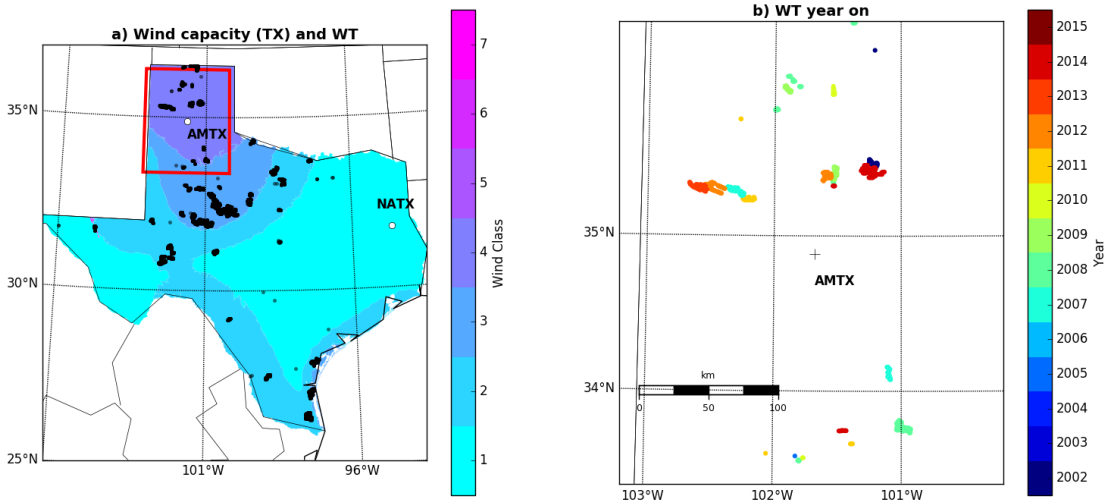

Figure 1: a) Wind capacity map for the state of Texas (US), location of wind turbines (Diffendorfer, Compton et al. 2017), and location of the two seismic stations used for testing the detection algorithm. b) Region around AMTX with WTs color-coded with the year on starting operations.

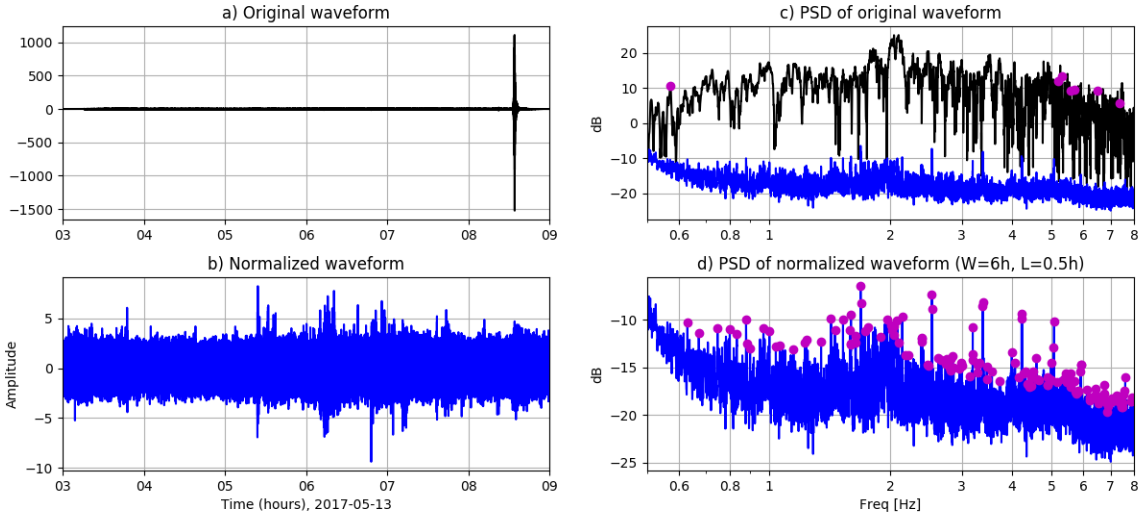

366 Figure 2: Temporal waveform normalization. The PSDs (panels b and d) were both

367 estimated using W=6 h and L=0.5 h, and 75% overlap between sub-windows.

368

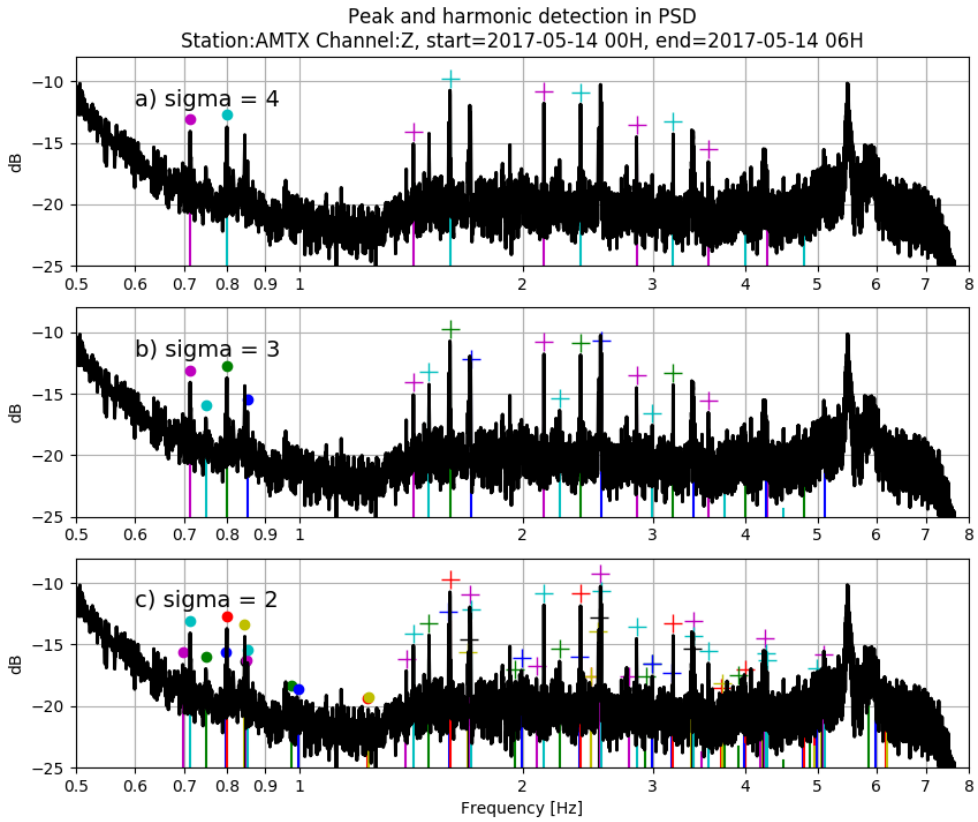

369

370 Figure 3: The influence of the number of standard deviations (s) in energy-peak

371 identification stage of the algorithm. The dots mark the location of the identified

372 fundamental frequency while the plus-symbols mark their harmonics. Fundamentals and

373 corresponding harmonics are linked by color. The colored vertical lines mark the

374 theoretical locations of harmonics at estimated fundamental frequencies.

375

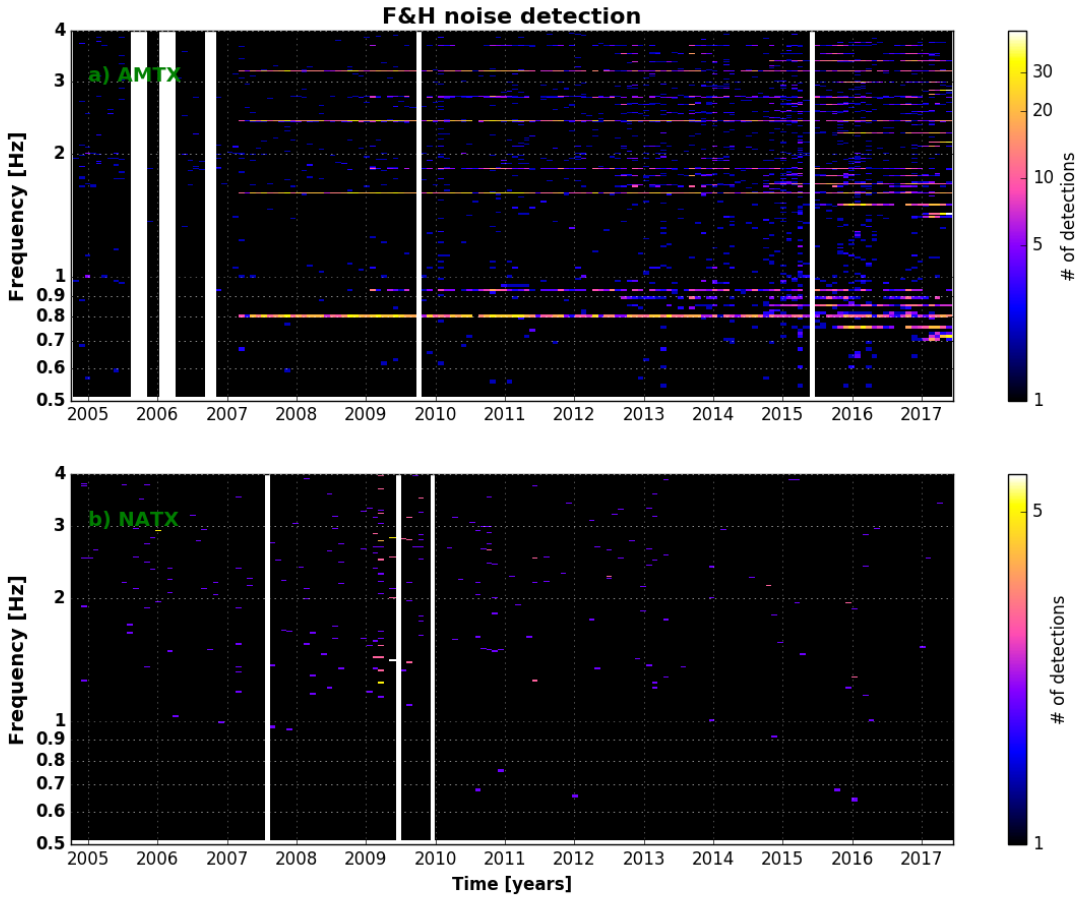

376

377 Figure 4: Detection of F&H noise for stations: AMTX and NATX since year 2005. The

378 Figure shows the number of detection in a 30-day period.

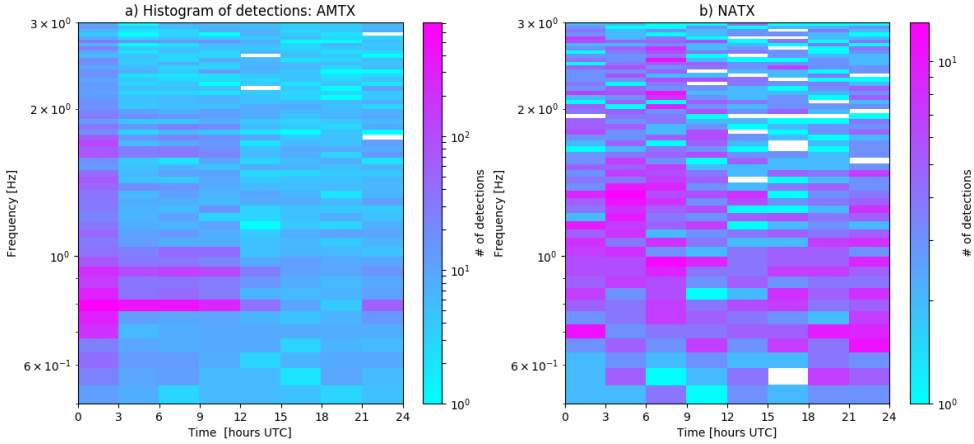

379

380

381 Figure 5: Distribution of peak detections by time of da

382

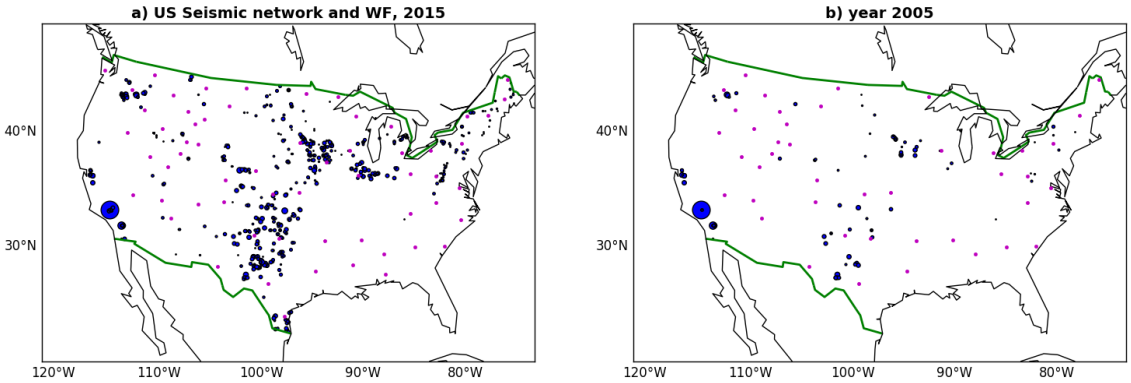

383

384 Figure 6: Distribution of energy plants (WTs with wind power capacity > 1 MW are

385 marked blue) and US Seismic Network stations (magenta dots) for years 2015 (a) and

386 2005 (b). The size of the blue circles is related to the relative amount of energy generated

387 by each power plant.

388

389

APPENDIX A

This electronic supplement develops several theoretical and practical aspects of implementing the spectral domain peak detector on seismic waveform data. The Waveform Temporal Normalization section documents the probability density function (PDF) for a general sample of the normalized waveform (Equation 1). In the Energy Peak Identification section, we derive the PDF for the peak value of the power spectral density (PSD), which is computed from the normalized time series. This problem is equivalent to a spectrogram peak detection problem in a limiting case. This limiting case provides a lower bound on the true detection probability of a signal with F&H noise. The Fundamental Harmonics Sequence Identification section then presents a simplified probability assessment of a sequence detection.

A.1 Waveform Temporal Normalization

We assume that the root-mean square (RMS)-normalization applied within our detector operates on raw waveform data d_i at time index i that are contaminated with zero mean Gaussian noise n_i of variance σ^2 that may include a nonzero signal s_i. The general distribution function for these data is:

$$d_i \sim \mathcal{N}(s_i, \sigma^2) \tag{A2}$$

where $\mathcal{N}(s_i, \sigma^2)$ describes a Gaussian distribution with mean s_i and variance σ^2. Data sample i has a probability density function (PDF) given by:

$$\mathrm{PDF}\{d_i\} = f_D(d_i) = \frac{1}{\sigma\sqrt{2\pi}} \exp\left[-\frac{(d_i - s_i)^2}{2\sigma^2}\right] \quad \text{(A3)}$$

412

413 The scaled, RMS sum of a $2N$-length vector of Gaussian distributed data samples $\overline{\boldsymbol{d}} =$
414 $\left[\bar{d}_0, \bar{d}_1, \ldots, \bar{d}_{2N-1}\right]$ is not Gaussian distributed; rather such a scalar will have a modified
415 chi distribution. However, when N is large enough, the Central Limit Theorem is
416 approximately applicable so that ω_i does have a Gaussian distribution. We perform
417 numerical experiments to investigate the distributional fit of a Gaussian PDF to binned
418 counts (histograms) ω_i. Figure A1 demonstrates that ω_i is effectively normal when $N =$
419 150 samples. We therefore proceed with our remaining analysis under the assumption
420 that ω_i is normally distributed, but remark that shorter processing windows ($N < 150$)
421 may require using the exact distributional form for ω_i. With this caveat, we now
422 estimate the distributional form for $\bar{d}_i$. From Equation A1 and Figure A1, both d_i and ω_i
423 are correlated (effectively) Gaussian random variables. This means that $\bar{d}_i$ has a ratio
424 distribution from correlated Gaussian data, where the denominator has a non-zero mean.
425 If d_i is not strongly correlated with ω_i, such data have an approximate, so-called Hinkley
426 distribution (Hinkley 1969). This distribution approximately normal under a functional
427 transformation (Geary 1930). However, this transformation becomes a multiplication by a
428 scalar when both the mean of the denominator is substantially larger than the mean of the
429 numerator, and when the variance of the denominator is substantially smaller than that of
430 the numerator. This implies that $\bar{d}_i$ is also effectively normal when such conditions are
431 met. Figure A2 shows a histogram of $\bar{d}_i$ that we computed from Equation A1 using
432 bandpass filtered, normally distributed noise. This histogram is superimposed with two

distinct curves that describe normal and Hinkley PDFs. These curves are effectively indistinguishable and provide an excellent match to the data histogram. The Figure A2 caption describes more processing details.

A.2 Energy Peak Identification (pure sinusoid, no harmonics)

Section Waveform Temporal Normalization demonstrates that $\bar{d}_i$ effectively has a normal distribution when waveform data are first normalized (Equation A1) using $N \geq 150$ and then filtered with a sufficiently wide-band filter. We therefore proceed under the assumption that our data $\bar{d}_i$ are Gaussian and find the PDF for the peak spectral energy. This problem is nearly equivalent to that treated elsewhere to detect an unknown sinusoid of unknown amplitude, phase, frequency and time of arrival (Kay 1998). The difference between this situation and our current application is that the Welch algorithm applied herein averages the amplitude spectral of a W-length data window over W/L constituent windows. This averaging operation has the effect of smoothing the mean amplitude spectra relative to that any segment's amplitude spectra. It is difficult to treat this general case, however, because the sum of several cosines with unknown arrival times (within a window) is complicated. We will therefore only treat the case where a harmonic signal (sinusoid) is completely contained within one of the L-length processing blocks. We also assume that there are many more processing blocks in this L length average that do not contain the sinusoid. Our resultant PDF therefore gives a lower bound on the peak detection performance of our algorithm.

The noisy sinusoid detection problem compares two competing hypotheses for the data that is localized within a given processing block included in the Welch algorithm:

$$\begin{aligned} &\mathcal{H}_0: d_i \sim \mathcal{N}(0, \sigma^2) \\ &\mathcal{H}_1: d_i \sim \mathcal{N}(A\cos(2\pi f_0 n + \varphi), \sigma^2) \end{aligned} \tag{A3}$$

Here, the sinusoid parameters and the block localization are unknown. We test these hypotheses not on d_i, but on $\bar{d}_i$ with a generalized likelihood ratio test. In practice, each Welch processing block contains an 2*N*-length sample vector of $\bar{d}_i$, or $\overline{\boldsymbol{d}} = [\bar{d}_0, \bar{d}_1, \ldots, \bar{d}_{2N-1}]$. This test then evaluates the PDF of $\overline{\boldsymbol{d}}$ at the maximum likelihood estimates of its unknown parameters under $\mathcal{H}_1$, and divides this PDF by the PDF of $\overline{\boldsymbol{d}}$ under $\mathcal{H}_0$; we assume for now that the background noise variance is well estimated and effectively known. The resultant test statistic

$$\max_{i,k} T_{i,k}(\overline{\boldsymbol{d}}) \tag{A4}$$

represents a sampled spectrogram $T(\overline{\boldsymbol{d}})$, evaluated at the frequency and processing block at which the spectrogram peaks. Specifically, index i represents the ith, *L*-length processing block of data points, k represents the kth frequency coefficient for the ith block of such data. The detector that decides a sinusoid is absent/present takes the form:

$$\max_{i,k} T_{i,k}(\overline{\boldsymbol{d}}) \underset{\mathcal{H}_0}{\overset{\mathcal{H}_1}{\lessgtr}} \gamma \tag{A5}$$

473

474 The statistic $\max_{i,k} T_{i,k}(\overline{\boldsymbol{d}})$ takes on a χ_2^2 distribution with a noncentrality parameter

475 conditional on the presence/absence of a sinusoid. The generalized likelihood ratio test

476 (Equation A5) represents a special case of the harmonic detection algorithm we present

477 here. The performance of these detectors is equivalent when a noisy sinusoid that

478 represents the signal from a wind farm is entirely contained within a single processing

479 block. The performance of this detector that describes the number of false detections

480 versus number of true detections is quantified by the distributional form of statistic

481 $\max_{i,k} T_{i,k}(\overline{\boldsymbol{d}})$. For low false alarm probabilities that satisfy $\mathrm{Pr}_{FA} < 10^{-2}$ (detector false

482 alarm probabilities are usually much lower), and if NB represents the number of

483 spectrogram processing blocks,

484

$$\mathrm{Pr}_{FA} = NB\left(\frac{L}{2} - 1\right)\exp\left(-\gamma/\sigma^2\right) \tag{A6}$$

485

486 The probability Pr_D of correctly detecting a sinusoid buried in noise and contained in a

487 single processing block is:

488

$$\mathrm{Pr}_D = F_{\chi_2^2(\lambda)}\left(2\ln\frac{NB\left(\frac{L}{2} - 1\right)}{\mathrm{Pr}_{FA}}\right) \tag{A7}$$

489

where $F_{\chi_2^2(\lambda)}$ is the $\chi_2^2(\lambda)$ is non-central chi-square probability distribution function (CDF) with 2 degrees of freedom with non-centrality parameter $\lambda = LA^2/2\sigma^2$. Equation A7 indicates that the sinusoid detection performance increases linearly with the number of data samples used in a processing block, and quadratically with the amplitude of that sinusoid. In practice, because spectrogram windows overlap adjacent samples are correlated. This reduces the effective size of NB and the true distribution for $\max_{i,k} T_{i,k}(\overline{\boldsymbol{d}})$ will be represented by a scaled $\chi_2^2(\lambda)$ distribution. Such scaling only modifies the PDF through an analogous scaling so that if $f_{\chi_2^2(\lambda)}(x)$ is the $\chi_2^2(\lambda)$ PDF, then $\frac{1}{|c|} f_{\chi_2^2(\lambda)}(\frac{x}{|c|})$ is its scaled PDF.

Figure A4 shows a particular spectrogram estimate that uses a low amplitude signal where $A = 2$, $f_0 = 1$ Hz, $\varphi = 0.45$, $\sigma^2 = 5/4$, and the sinusoid duration was 30 seconds out of a total of 500 seconds of recording time (like that shown in Figure A3). Figure A5 shows the result of binning peak detections on 10^4 realizations of spectrograms like that shown in Figure A4. These realizations provide an excellent agreement to a scaled $\chi_2^2(\lambda)$ distribution, where the unknown scaling constant $|c| = 0.82$, and $\lambda = 450$. We conclude from this exercise that the probabilistic model summarized through Equations A3-A7 provides a reasonable approximation to the harmonic peak detection problem in the case that a sinusoid of sufficiently short duration is processed. Longer duration signals will only increase the probability of detection. Our analysis thereby provides lower bound on the true detection probability of a more persistent, longer duration sinusoidal signal.

Figure A6 illustrates a receiver operating characteristic (ROC) curve that quantifies the probability Pr_D of detecting a noisy sinusoid versus a ratio that measures the amplitude A of that sinusoid relative to background noise standard deviation, as measured by ratio A/σ. This ROC curve provides a lower bound on the expected detection performance of our detection algorithm. It shows that a sinusoid with an amplitude that is half the amplitude of the noise variability (σ) has greater than a 0.98 probability of being detected, even when the duration of that signal occupies only 6% of the temporal duration of the total record. Longer duration sinusoids with a similar signal power are therefore detectable with higher probability.

A.3 Fundamental harmonics (F&H) Sequence Identification

To quantify the ability of our detector to identify such sequences, we now consider a class of different signals than those we exploited in our prior analyses. In particular, our previous sections quantified the detector's capability to identify sinusoids buried in noise. Our treatment included pure sinusoids and therefore did not model waveforms that produce finite amplitude harmonics. It is difficult to analytically model waveform data that includes harmonics, that requires periodic, sinusoidal distortion. Because of this general difficulty, we will only treat a case whereby we prescribe the height of consecutive harmonic peaks. We concede that a complete approach would include modeling a realistic, periodic signal that produces harmonics (e.g., a van der Pol oscillator solution), but such an explicit description is unnecessary for testing our detector. In particular, we simply consider harmonic peaks to decay linearly with

harmonic index. This means that if the true fundamental has amplitude A_0^2 (in spectrogram space), a harmonic with index n has amplitude:

$$A_n^2 = \beta \frac{A_0^2}{n}, \qquad n = 1,2, \ldots, N \tag{A7}$$

where β is a (positive) decay rate. The particular value of the decay rate β is non-uniquely conditioned on the waveforms generated by a particular wind farm.

To estimate a harmonic sequence detection rates, we use the data we already generated to produce Figure A6. We then compute the unconditioned n^{th} harmonic's detection probability $\mathrm{Pr}_D^{(n)}$ by mapping fundamental detection probabilities shown at values of A_0^2/σ^2 to new SNR values A_n^2/σ^2, where $\mathrm{Pr}_D^{(0)}$ is the probability of detecting a fundamental. For example, if $n = 1$, $A_0^2/\sigma^2 = 1$, and $\beta = 0.4$, then $A_n^2/\sigma^2 = 0.4$ and we estimate $\mathrm{Pr}_D^{(1)} \approx 0.8$ from Figure 2 (note $\mathrm{Pr}_D^{(0)} \approx 1$, here). Such an unconditional probability in more general examples is distinct from the conditional probability that a harmonic was detected, given a fundamental peak was first detected. However, if detection probabilities are sufficiently independent, the probability Pr_D of detecting both a fundamental and harmonics are equivalent to the product of their probabilities so that:

$$\mathrm{Pr}_D = \mathrm{Pr}_D^{(0)} \mathrm{Pr}_D^{(1)} \tag{A8}$$

For ease of computation, we shall make the assumption that these probabilities are independent. This assumption approximately holds when waveform data are not correlated over long temporal durations (or equivalently, several adjacent frequency bins).

Our more general analysis is shown in Figure A7. We fixed $\eta = 2$ for consistency with Figure 3, and considered different values of β. Lower harmonic peaks, relative to that of the fundamental, show substantially lower sequence detection rates. These curves again form a lower bound on the true performance of our detector.

References

Geary, Robert Charles. "The frequency distribution of the quotient of two normal variates." *Journal of the Royal Statistical Society* 93.3 (1930): 442-446.

Hinkley, David V. "On the ratio of two correlated normal random variables." *Biometrika* 56.3 (1969): 635-639.

Kay, Steven M. "Fundamentals of Statistical Signal Processing, Volume 2: Detection Theory, ser." *Prentice Hall Signal Processing Series, AV Oppenheim, Ed. Prentice Hall PTR* (1998).

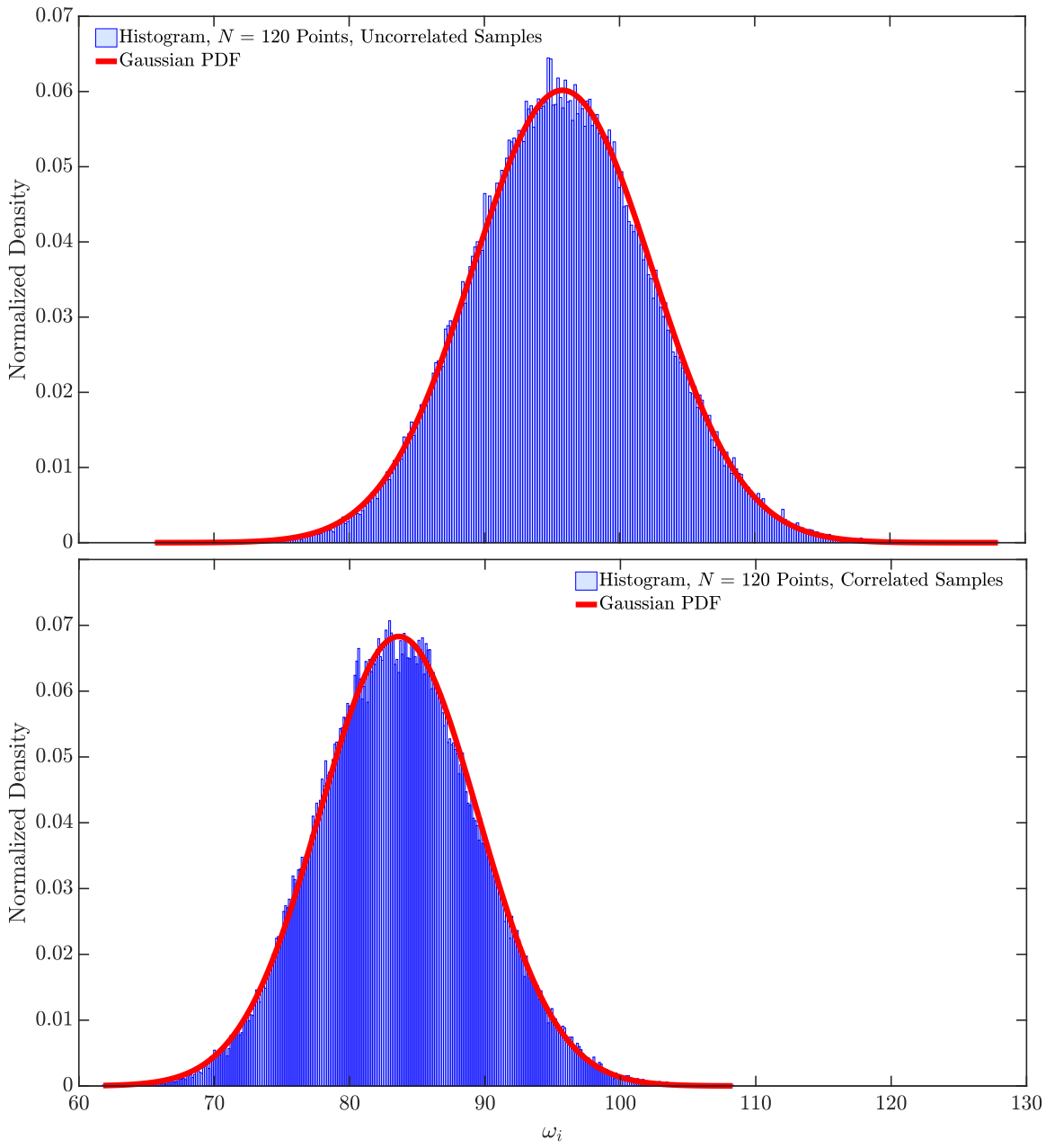

574

575 **Figure A1** Numerical experiments that test the normal distributional fit of ω_i using
576 uncorrelated (Top) and correlated (Bottom) data. We first applied Equation A1 to two
577 time series containing normally distributed noise. The first data set contained
578 uncorrelated data, whereas we filtered the second time series so that the samples were
579 highly correlated. We then binned these data (purple histograms) and fit them to normal
580 distributions (red curves). Our results demonstrate that ω_i is effectively normal. All
581 computations were performed in MATLAB.

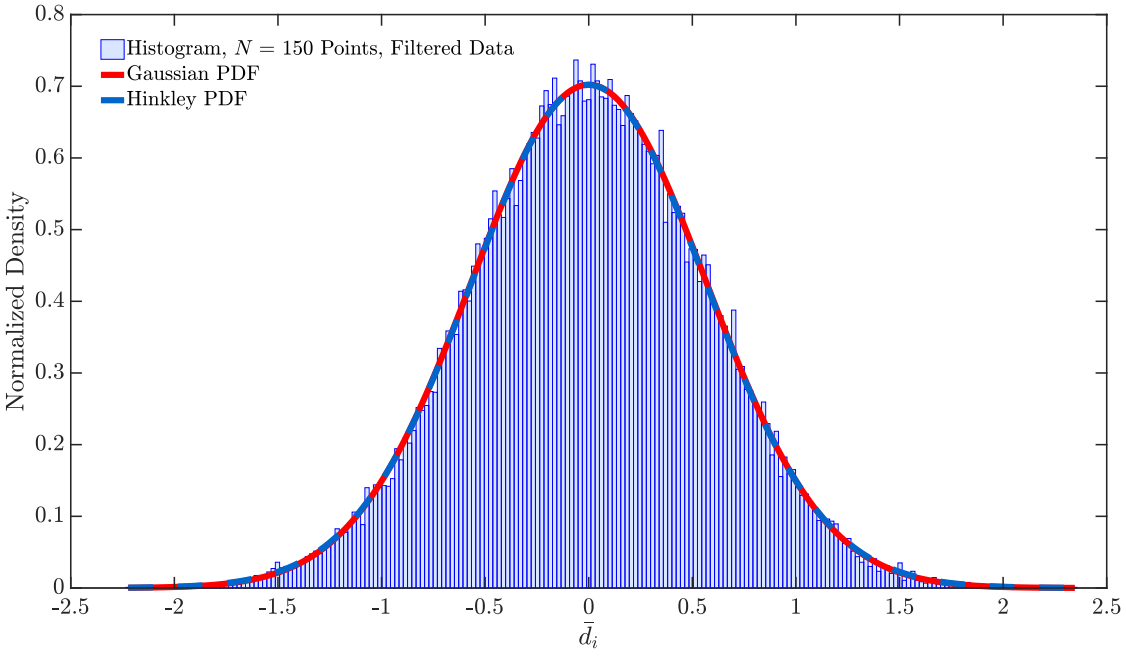

582

583 **Figure A2** A comparison between a normalized histogram (light blue) of $\widetilde{d}_i$ (Equation
584 A1) computed from bandpass filtered data, and two probability density functions (PDFs).
585 We used $N = 150$ samples and a fourth order, Butterworth filter with a pass band of [0.5,
586 5] Hz. The Hinkely PDF (blue) and normal PDF (red) both fit the data histogram very
587 well and are visually indistinguishable from each other at this scale. Additional
588 experiments with more filters demonstrate that our fits improve with increasing spectral
589 width. We conclude that $\bar{d}_i$ is reasonably described as a Gaussian random variable.

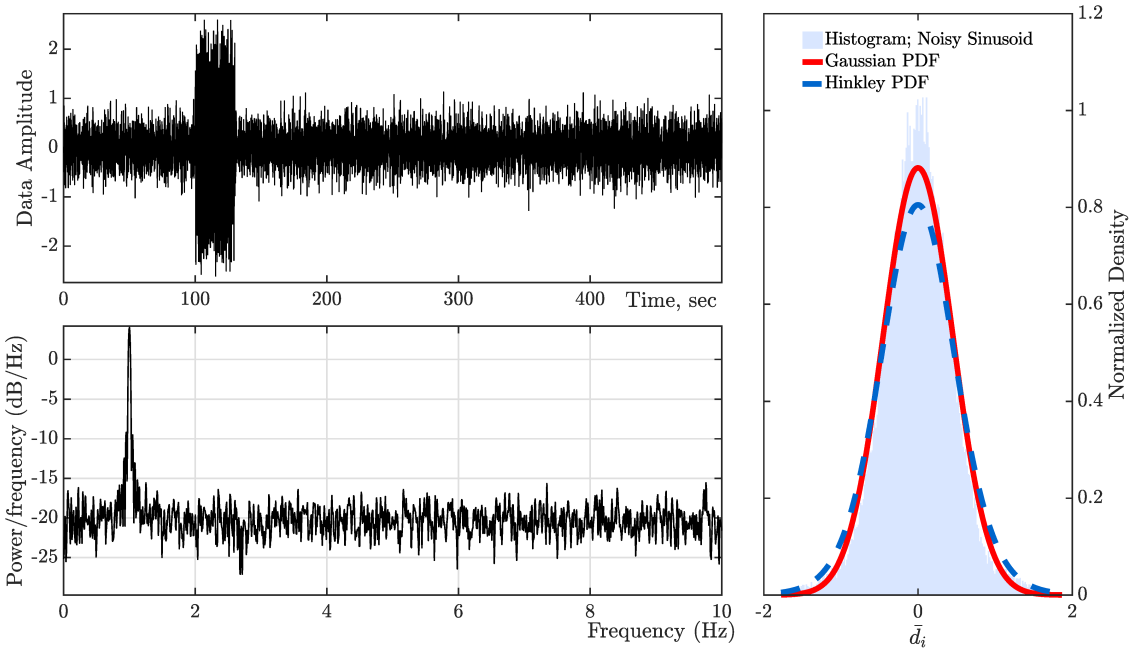

590

591 **Figure A3** Top, left: a band pass filtered signal d_i $(i = 0,1, \ldots, 5 \cdot 10^4)$ that contains a
592 sinusoid pulse with a 30 second duration. Bottom, left: a truncated portion of the
593 amplitude spectra of $\bar{d}_i$(Equation A1). Right: A histogram of $\bar{d}_i$ superimposed with two
594 PDF curves that show a Hinkley distribution (blue) versus a Gaussian distribution (red).
595 Both distributions provide reasonable fits to the data.

596

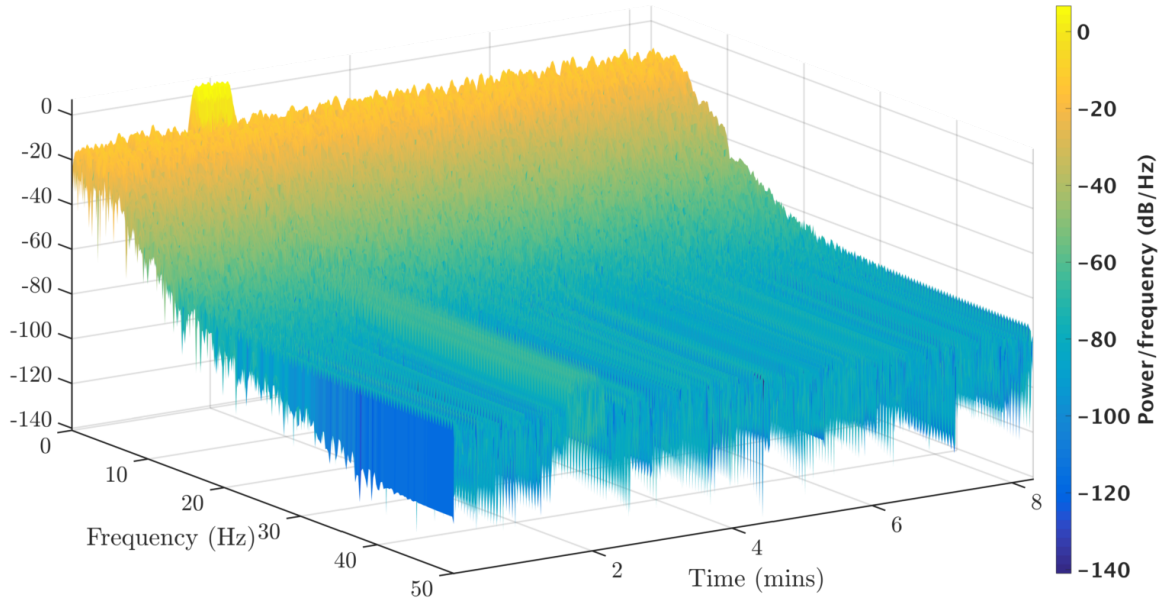

Figure A4 A spectrogram computed from time series like that depicted in Figure A3.

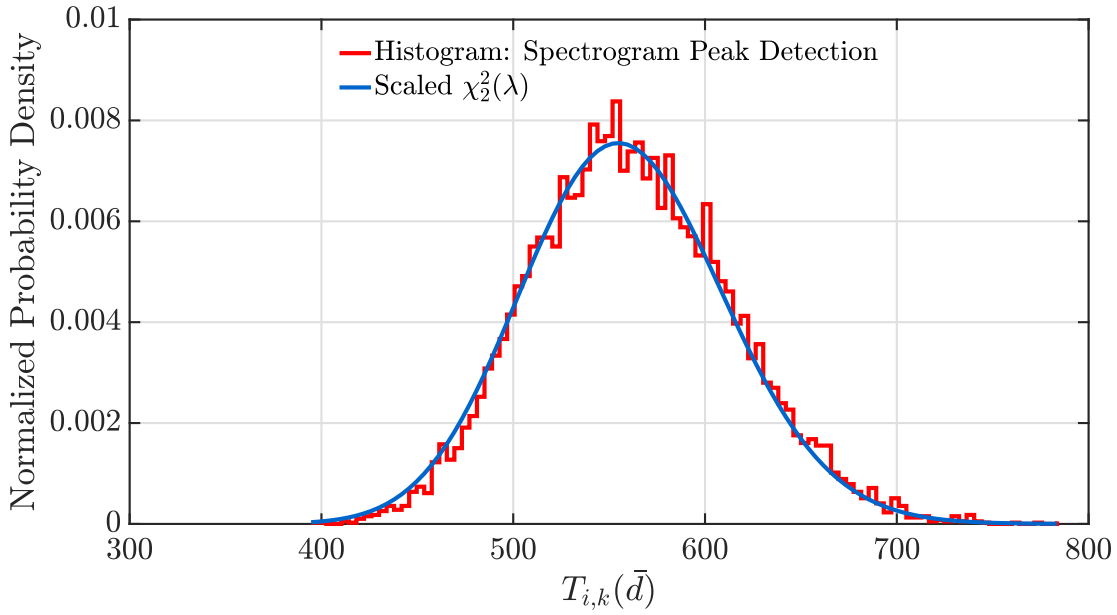

Figure A5 A histogram computed from 10^4 peak spectrogram detections using data like that shown in Figure A4 (red) superimposed with a scaled $\chi_2^2(\lambda)$ PDF (blue). This simulation suggest that $\max_{i,k} T_{i,k}(\bar{\boldsymbol{d}})$ (Equation) is effectively $\chi_2^2(\lambda)$ distributed when the detector processes a noisy harmonic signal that is triggered by wind farm fans.

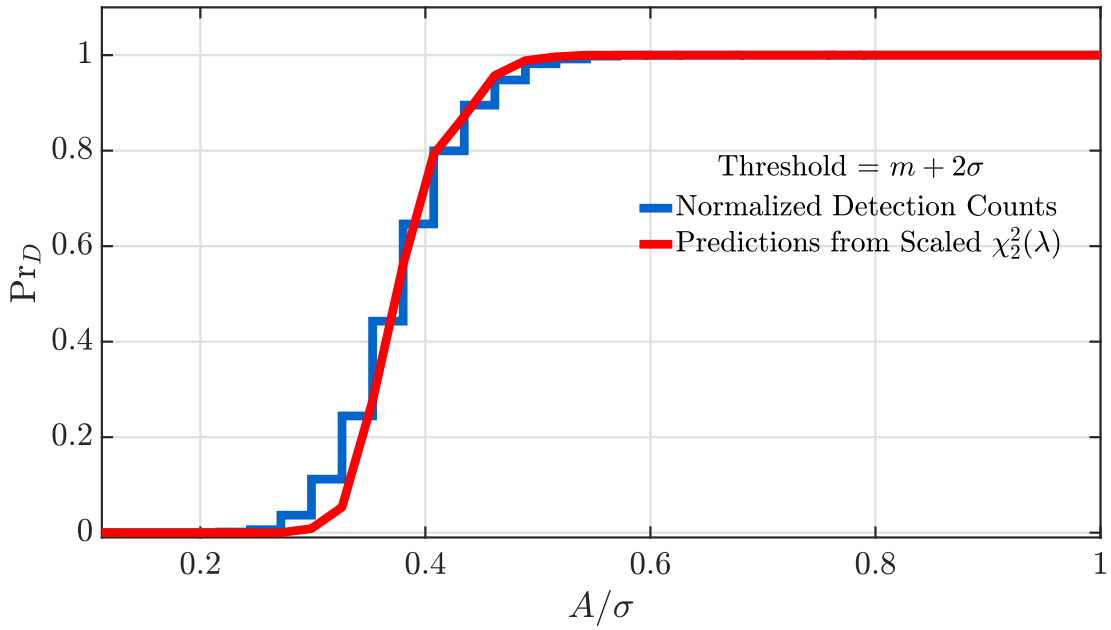

Figure A6 Simulated empirical (blue) and theoretical (red) ROC curves that quantify the detector's capability to identify peaks in spectrograms. The curves measure the detection probability $\Pr_D$ versus the ratio of signal amplitude to noise variability, as measured by A/σ. The curves demonstrate that the detection algorithm matches predicted detections with filtered and processed input signals like that shown in Figure A3 and Figure A4. We constructed the threshold in the present case using $m = 2$ and $\sigma \approx 1.15$. These ROC curves present a lower bound on the detection capability of our detector because they quantify detection rates for noisy sinusoids with temporal durations that are short relative to that of the detector's processing window.

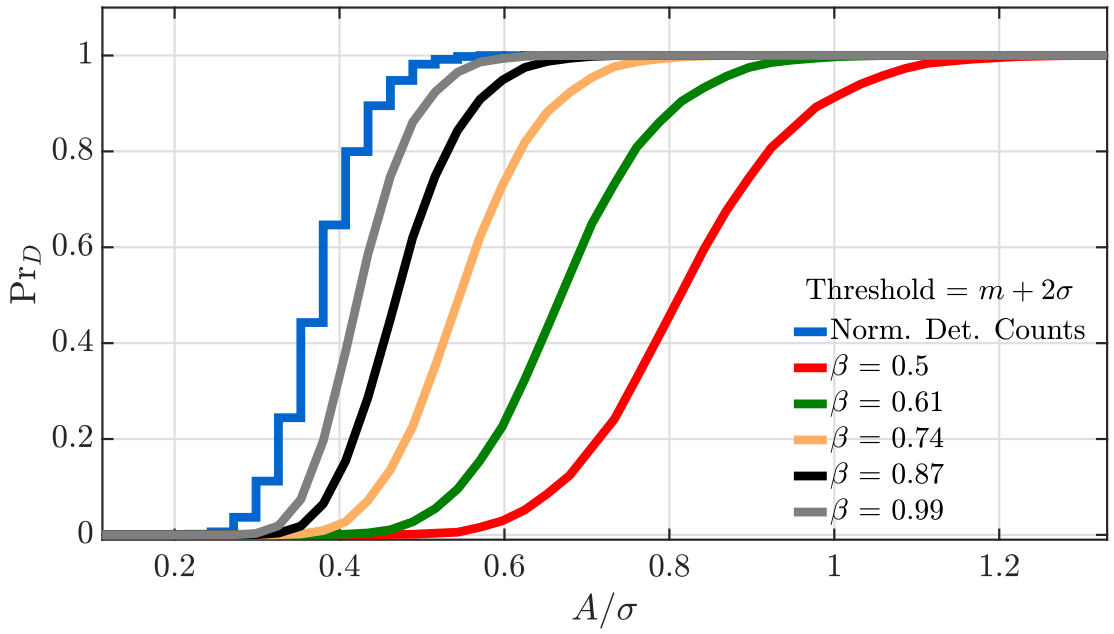

618

619 **Figure A7** A family of ROCs curves that quantify a detector's capability $\Pr_D =$

620 $\Pr_D^{(0)} \Pr_D^{(1)}$ to identify a periodic signal's fundamental frequency and its first harmonic

621 (Equation A8). It shows the detection probability $\Pr_D$ versus the ratio of signal amplitude

622 to noise variability, as measured by A/σ, assuming $A_n^2 = \beta \frac{A_0^2}{n}$ ($n = 1$, here). When

623 $A_0^2/A_1^2 = 1/2$, the detection rate for both the fundamental and its first harmonic reduces

624 from $\Pr_D \approx 1$ for just the fundamental to $\Pr_D \approx 0.5$ for a detection of both the

625 fundamental and the first harmonic. We used the same threshold for detection as used in

626 Figure A6.

627